Supporting Information

Jiao et al. 10.1073/pnas.1105296108

SI Materials and Methods

In Vitro Slice Preparation. Mice (P10–P30) were deeply anesthetized with pentobarbital sodium (55 mg/kg) and decapitated. We adopted a slice preparation with a modified angle. The modification was made based on the results of Land and Kandler in rat slices (1), Briefly, we first made a cut right to the sagittal plane. Next, the brain was rotated counterclockwise with the caudal side up. The rostral end of the brain was glued to a Vibratome. Brain slices were collected based on anatomical features (e.g., hippocampus and TC fibers). A maximum of two slices (250 μm) were collected that contained rows A through E of posterior medial barrel subfield, with the D/E row located right above the hippocampus region on the most lateral side of the slice. Slices were regularly stained with CO and subsequently reconstructed to verify the location of barrels. Whisker trimming at P7 consistently induced a reduction in the intensity of CO or vGluT2 in DE, which can be used to validate the location of DE row. The brain slice cutting method was based on a previous publication (2).

Whole-Cell Patch-Clamp Recording of IPSCs from Spiny Neurons. Patch pipette solution was modified according to previous reports (2, 3) and was composed of (in mM): 100 Cs-gluconate, 10.0 phosphocreatine-Tris, 3.0 $MgCl_2$, 0.07 $CaCl_2$, 4 EGTA, 10.0 Hepes, 4.0 Na2-ATP, and 1.0 Na-GTP, pH adjusted to 7.4, and osmolarity adjusted to 280 mosM L^{-1}.

Separation of Excitatory and Inhibitory Conductances. The method we used was based on the continuous measurement of conductance dynamics during stimulus-evoked synaptic response. This method was primarily used in vivo on cat cortex (4). The excitatory and inhibitory conductance underlying the mixed synaptic responses were extracted by using the equations that were previously described by Cruikshank et al. (5). In the present study, synaptic current was determined for each holding potential (three potentials were used for the analysis). We plotted a synaptic I/V curve at each time point and fitted these plots with linear regression. Based on the slopes and voltage intercepts, we calculated G_{syn} and E_{syn}, respectively. Continuous conductance and reversal potential waveforms were constructed. Holding potentials were corrected for a calculated liquid junction potential of 12 mV, which was similar to previous studies. E_e was 0 mV and E_i was –60 mV. G_{syn} was then separated into G_e and G_i, which were also plotted as continuous waveforms (Fig. 3). To validate our methods, we also measured G_e and G_i when the excitatory or inhibitory synapses were blocked by 10 μM NBQX or 50 μM picrotoxin, respectively (Fig. S2).

CO Histochemistry. Methods for CO staining were adapted from the method published by Wong-Riley (6)).

Western Blotting. Freshly dissected barrel cortex from P30 mice was immediately homogenized in ice-chilled RIPA buffer and was processed for Western blotting based methods described earlier (7). Antibodies used were polyclonal anti-BDNF antibody (1:200; no. SC546; Santa Cruz Biotechnology) and an anti-human BDNF pAb (1:3,000; no. 500-p84; Peprotech). Specificity of these two BDNF antibodies has been examined in previous studies (8–10) and confirmed here with recombinant human BDNF (no. 450–02; Peprotech) and proBDNF (Alomone Labs).

BDNF Protein Quantification with ELISA. Total BDNF (proBDNF plus mBDNF) was measured by using the BDNF Emax ImmunoAssay System (Promega) with a Tecan Infinite 200 microplate reader (absorbance, 450 ± 9 nm).

Quantification of Inhibitory Presynaptic Boutons and PV Expression. A Zeiss Axioskop 2FS microscope, equipped with a 100× oil immersion plan achromatic objective and a 10× objective lens, was used to count the number of perisomatic boutons. The microscope was equipped with a CCD video camera and was connected to the NeuroExplorer program (MicroBrightField). With a 10× objective lens, we first identified and outlined the deprived row and spared row, and then switched to a 100× objective lens. The number of perisomatic boutons was counted in defined regions in individual sections. Perisomatic inhibitory varicosities were defined as small (0.5–1-μm) GFP-positive puncta located within 1 μm of a GFP-negative cell body. Confocal microscopy was performed in the University of Wyoming Microscopy Core Facility. An upright Nikon E800 microscope was used as confocal laser scanning microscope (Radiance 2100; Bio-Rad). Laser lines includes blue diode laser (405 nm), argon ion laser (457, 477, 488, and 514 nm), HeNe Laser (543 nm), and red diode laser (637 nm). AxioVision LE imaging suite software, and its automeasure program, were used to study synaptic bouton densities near a spiny neuron.

Image Digital Processing. Confocal and epifluorescent images were digitally processed with Photoshop CS4 (Adobe) and IGOR pro (Wavemetrics). After the image was imported, the LineProfile operation was used to sample the image along a path consisting of an arbitrary number of line segments and provides mean grayscale value for all pixels along the line segments. The ΔG values for BDNF IR between barrels and septum were determined by measuring mean grayscale values in barrels and septum area determined by CO staining in adjacent sections. Cross-correlation analysis was performed by using Clampfit 10 (Molecular Devices), whereby grayscale line profile values for two intrinsic signals (PV and GFP) were analyzed with cross-correlation analysis and a cross-correlation coefficient value was obtained, with a value of 1 meaning complete correlation between the two curves (i.e., identical).

1. Land PW, Kandler K (2002) Somatotopic organization of rat thalamocortical slices. *J Neurosci Methods* 119:15–21.
2. Sun QQ, Huguenard JR, Prince DA (2006) Barrel cortex microcircuits: Thalamocortical feedforward inhibition in spiny stellate cells is mediated by a small number of fast-spiking interneurons. *J Neurosci* 26:1219–1230.
3. Sun QQ (2009) Experience-dependent intrinsic plasticity in interneurons of barrel cortex layer IV. *J Neurophysiol* 102:2955–2973.
4. Borg-Graham L, Monier C, Frégnac Y (1996) Voltage-clamp measurement of visually-evoked conductances with whole-cell patch recordings in primary visual cortex. *J Physiol Paris* 90:185–188.
5. Cruikshank SJ, Lewis TJ, Connors BW (2007) Synaptic basis for intense thalamocortical activation of feedforward inhibitory cells in neocortex. *Nat Neurosci* 10:462–468.
6. Wong-Riley MT, Welt C (1980) Histochemical changes in cytochrome oxidase of cortical barrels after vibrissal removal in neonatal and adult mice. *Proc Natl Acad Sci USA* 77:2333–2337.
7. Sakata K, et al. (2009) Critical role of promoter IV-driven BDNF transcription in GABAergic transmission and synaptic plasticity in the prefrontal cortex. *Proc Natl Acad Sci USA* 106:5942–5947.
8. Causing CG, et al. (1997) Synaptic innervation density is regulated by neuron-derived BDNF. *Neuron* 18:257–267.
9. Yang J, et al. (2009) Neuronal release of proBDNF. *Nat Neurosci* 12:113–115.
10. Zhang Z, Jiao YY, Sun QQ (2011) Developmental maturation of excitation and inhibition balance in principal neurons across four layers of somatosensory cortex. *Neuroscience* 174:10–25.

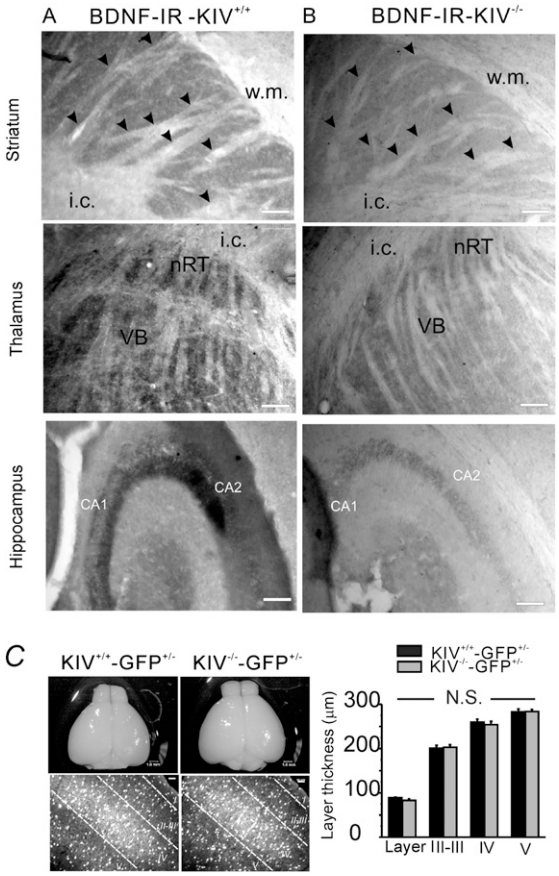

Fig. S1. BDNF IR in different subcortical regions in KIV$^{+/+}$-GFP$^{+/-}$ and KIV$^{-/-}$-GFP$^{+/-}$ mice. Photomicrographs of BDNF IR in striatum (*Upper*), thalamus (*Middle*), and hippocampus (*Lower*) of KIV$^{+/+}$-GFP$^{+/-}$ (*A*) and KIV$^{-/-}$-GFP$^{+/-}$ (*B*) mice (n = 4 mice in each condition). w.m., white matter; I.C., internal capsule; nRT, nucleus reticularis of thalamus; VB, ventral basal complex of thalamus. (Scale bar: 100 μm.) Note that BDNF IR was found in thalamic relay nucleus of thalamus but not in the TC axons (*Top*), indicating cortical BDNF IR is local. (*C*) Comparison of gross cortical cytoarchitectonic structures and brain size in KIV$^{-/-}$-GFP$^{+/-}$ and KIV$^{+/+}$-GFP$^{+/-}$ littermates. (Scale bars in: 1 mm for the whole-brain and 50 μm for the slice image, respectively.)

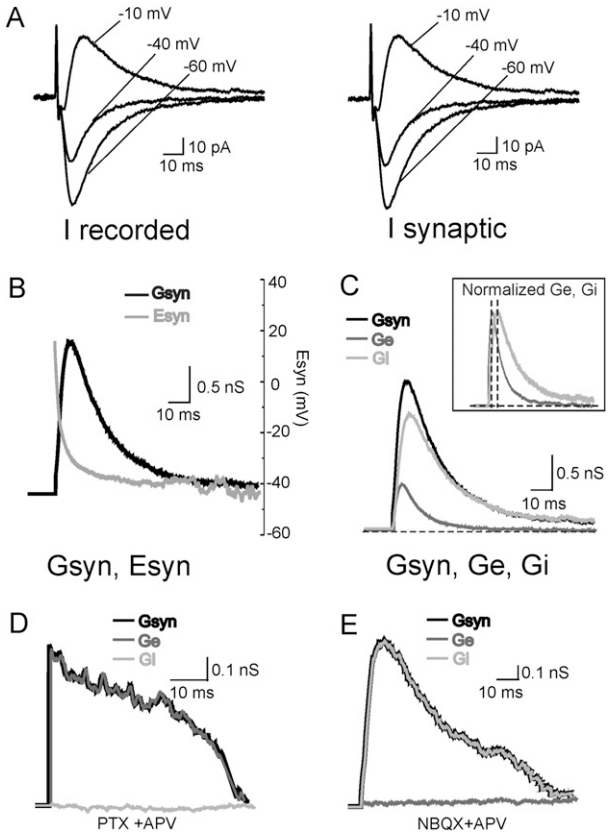

Fig. S2. Separation and validation of excitatory and inhibitory conductances. (*A*) *Left*: Actual recording of postsynaptic current ($I_{recorded}$) evoked by local stimulation at three holding potentials (−10, −40, −60 mV). Traces are means of 10 consecutive sweeps. *Right:* Synaptic currents (I_{syn}) reconstructed by subtracting baseline currents from the traces on the left. (*B*) Continuous plots of G_{syn} and E_{syn}. (*C*) Continuous plots of G_{syn} and G_e and G_i components of the total G_{syn}. *Inset*: Normalized G_e and G_i. Note that G_e peaked 3.6 ms before G_i (dashed lines). (*D*) Complete elimination of G_i after blocking $GABA_A$ receptors [picrotoxin (PTX)] and NMDA receptors [D-(−)-2-amino-5-phosphonopentanoic acid (APV)]. (*E*) Complete elimination of G_e after blocking AMPA receptors [2,3-dioxo-6-nitro-1,2,3,4-tetrahydr obenzo[f]quinoxaline-7-sulfonamide (NBQX)] and NMDA receptors (APV).

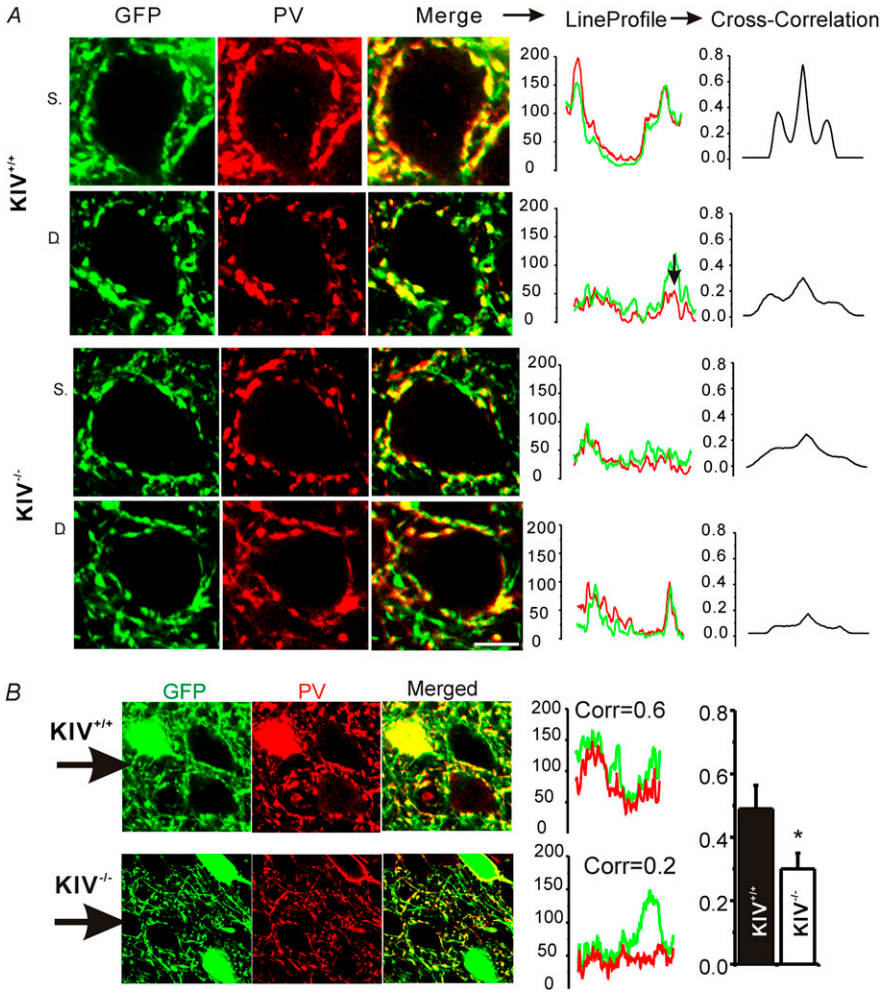

Fig. S3. Lack of sensory deprivation induced structural plasticity in KIV$^{-/-}$-GFP$^{+/-}$ mice. (*A*) Representative confocal photomicrograph examples of GFP IR and PV IR in layer IV barrel cortex from spared (S) rows (C through A rows in which whiskers were intact) and deprived rows (D, D/E rows of row -trimmed mice). (Scale bars: 2 μm.) For each merged image, profile of the entire image for PV (red) and GFP (green) and the cross-correlation plot for line profile curves are shown on the right. (*B*) Confocal images of PV (red) and GFP (green) and profile across the entire image for PV (red) and GFP (green), respectively. Corr, cross-correlation coefficient of the red (PV) and green (GFP) channels. *Right*: Bar graph shows plot of cross-correlation in KIV$^{+/+}$ versus KIV$^{-/-}$ mice (n = 4 brains in each group).